Supporting Information

Switchable Sensor and Scavenger: Detection and Removal of Fluorinated Chemical Species by Luminescent Metal-Organic Framework

Hua-Qing Yin,[a,b,c] Kui Tan,[d] Stephanie Jensen,[e] Simon J. Teat,[f] Saif Ullah,[e] Xiuze Hei,[a] Ever Velasco,[a] Kolade Oyekan,[d] Noah Meyer,[e] Xin-Yao Wang,[b] Timo Thonhauser,[e] Xue-Bo Yin,*[,b] Jing Li*[,a]

[a]Department of Chemistry and Chemical Biology, Rutgers University, 123 Bevier Road, Piscataway, NJ 08854, United States.

[b]State Key Laboratory of Medicinal Chemical Biology, Tianjin Key Laboratory of Biosensing and Molecular Recognition, College of Chemistry, Nankai University, 94 Weijin Road, Tianjin 300071, China.

[c]Institute for New Energy Materials and Low Carbon Technologies, School of Materials Science & Engineering, Tianjin University of Technology, 391 Bin Shui Xi Dao Road, Tianjin 300384, China.

[d]Materials Science and engineering, the University of Texas at Dallas, 800 W. Campbell Road, Richardson, TX 75080, United States.

[e] Department of Physics and Center for Functional Materials, Wake Forest University, 1834 Wake Forest Road, Winston-Salem, NC 27109, United States.

[f]Advanced Light Source, Lawrence Berkeley National Laboratory, 1 Cyclotron Road, Berkeley, CA 94720, United States.

S1. Starting Materials

All reagents and solvents were used as received from the following vendors: Methyl 4-formylbenzoate (98%) were purchased from HWRK Chem Co., Ltd., Beijing, China. Ammonium acetate bought from JBT Aker Inc. Sodium fluoride (99%) got from Aldrich Chemical Company Inc., US. Sodium hydroxide (98%) purchased from Signa-Aldrich. Perfluorooctanoic acid (96%), acetic anhydride (99%), Vitamin B1 (98%), anhydrous indium chloride (≥99%) purchased from Alfa-Aesar. 1,2,4,5-Tetrakis(4-carboxyphenyl)benzene (H_4tcpb) was bought from Kaiyulin Chem. Co., Ltd. Shanghai China. 2,3,5,6-Tetrakis(4-carboxyphenyl)pyrazine (H_4tcpp) was synthesized by the reported method.[1]

Ice acetic acid (99%), tetrahydrofuran (99%), diethyl ether (98%), methanol (99.9%), ethanol (99.8%), *N, N'*-dimethylacetamide (DMA, 99%) and formic acid got from VWR Scientific Inc., US. Ultrapure, deionized water was obtained through a Direct-Q Water Purification System (EMD Millipore) at a 0.5 L min^{-1} flow rate, and was used for all detection and uptake experiments.

S2. Instruments and Material Characterization

2.1 N_2 sorption measurements

N_2 adsorption isotherms of outgassed In(tcpp) or In(tcpb) were collected on a Quantachrome Instruments Autosorb-1 MP volumetric gas sorption analyzer using ultra high purity nitrogen gas (99.999%). Liquid nitrogen was used as coolant to achieve cryogenic temperature (77 K). The N_2 isotherms were collected in a pressure range from 10^{-7} to 1 atm. The pore-size distribution was calculated by BJH method using a DFT program.

2.2 Thermogravimetric analyses (TGA)

TGA was performed using a TA Instrument Q5000 under constant N_2 flow (20 mL min^{-1}). Approximately 3 mg of sample was placed into a platinum pan, which was then heated from 50 - 600 °C at a rate of 10 °C min^{-1}.

2.3 Fourier transform infrared (FTIR) spectra

FTIR spectra were obtained by Bruker TENSOR 27 Fourier transform infrared spectroscopy. The FTIR spectroscopy was used to identify the different functional groups in H_4tcpp, In(tcpp), and the In(tcpp) exposed in the F^- and PFOA. For these measurements, the powder was gently pressed onto a KBr pellet

(~1 cm diameter, 1-2 mm thick) for FTIR analysis.

2.4 Structural analysis of In(tcpp)

Single crystal X-ray diffraction data for In(tcpp) were collected on a Bruker D8 diffractometer with PHOTON 100 detector using the synchrotron source (λ = 0.7749 Å) at the Advanced Light Source 11.3.1 Chemical Crystallography beamline (Table 1). All non-hydrogen atoms were refined anisotropically; hydrogen atoms were placed geometrically, constrained, and refined with a riding model.

2.5 Powder X-ray Diffraction (PXRD) analysis

PXRD analyses were performed using a Rigaku Ultima-IV- diffractometer at room temperature under Cu Kα radiation (λ = 1.5406 Å). Data were collected 3 - 37.5° 2θ, with the operating power set to 40 Kv/44 Ma. The scan rate was 2° 2θ min^{-1}, with a step size of 0.02° 2θ.

2.6 UV-visible diffuse reflectance spectra

UV-vis spectra were obtained for the as mentioned in solid or liquid state at room temperature using Shimadzu UV-3600 spectrophotometer.

2.7 Luminescence spectra and internal quantum yield

Using a Varian Cary Eclipse spectrophotometer, excitation and emission spectra were collected for as-made, activated solid samples and liquid samples of MOFs and ligands. Absolute internal quantum yield (IQY) in solid state was measured using a Hamamatsu C9220-03 spectrophotometer with integrating sphere.

S3. DFT Calculation Details

Calculations were performed at the DFT level in VASP[2, 3] with the vdW-DF exchange-correlation functional[4-7] in order to capture the long-range van der Waals interactions between the guest molecules (PFOA, NaF, and HF) and both the In(tcpp) frameworks. Optimizations were performed until SCF loops reached an energy convergence of $1x10^{-5}$ eV and forces were below 1 meV/ Å for each atom. Only the Γ-point was considered with a plane-wave energy cutoff of 600 eV. To calculate photoluminescence intensity, we calculate the oscillator strength (f_{ij}) as follows:[8, 9]

$$f_{ij}\left(\{R_I(t)\}\right) = e\frac{4\pi m_e \omega_{ij}}{3\hbar e^2}\left|D_{ij}\left(\{R_I(t)\}\right)\right|^2$$

$$D_{ij}(\{R_I(t)\}) = e\int \psi_i^*(\{R_I(t)\})\, r\, \psi_j(\{R_I(t)\})\, d^3r$$

where e and m_e are the charge and mass of the electron, $\hbar\omega_{ij} = \varepsilon_i - \varepsilon_j$ is the energy difference between electronic states i and j, $\{\mathbf{R}_I(t)\}$ is the set of all ionic positions at time t, and $\mathbf{D}_{ij}$ is the transition dipole moment. The oscillator strength gives us the probability of an optical transition occurring. To model photoluminescence, we run *ab initio* molecular dynamics (AIMD) at room temperature after a 200-fs thermalization. A 1-fs time step is used for a 1-ps trajectory, giving 1000 data points of photoluminescence intensity by using the normalized oscillator strength values for intensity. It is important to note that this methodology cannot capture photoluminescence due to exciton formation. We use the scissor rs operator to match the experimentally observed optical band gap of 400 nm for In(tcpp) as DFT is known to underestimate band gaps. Full computational details for this methodology to model photoluminescence is reported elsewhere.[10] Vibrational modes and frequencies for the F@In(tcpp) model were calculated using a finite differences method in VASP with a displacement of 0.01 Å.

For F@In(tcpp) DFT calculation the guests are sufficiently small to use the primitive unit cell (64 atoms). Because F^- is experimentally introduced into the MOF as NaF salt, both Na^+ and F^- are included in the model. Numerous starting configurations of Na^+, F^-, and Na^+F^- were tested.

For PFOA@In(tcpp) the size of the PFOA molecule necessitates the use of supercells of In(tcpp) in order to model the 6 different ways PFOA could fit inside the MOF pores. Both a 2 × 1 × 1 and 1 × 2 × 1 supercell (128 atoms) were implemented, and only 2 of the models showed an energetically favorable binding energy (calculated as $E_{binding} = E_{PFOA@In(tcpp)} - E_{PFOA} - E_{MOF}$). Both favorable models were in the 2×1×1 supercell and had nearly identical energetic favorability.

S4. Figures and Tables

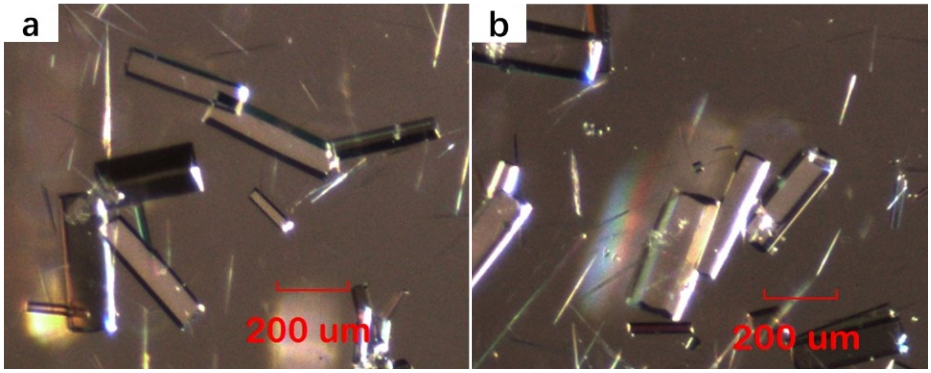

Fig. S1 Crystal images of (a) In(tcpp) and (b) In(tcpb).

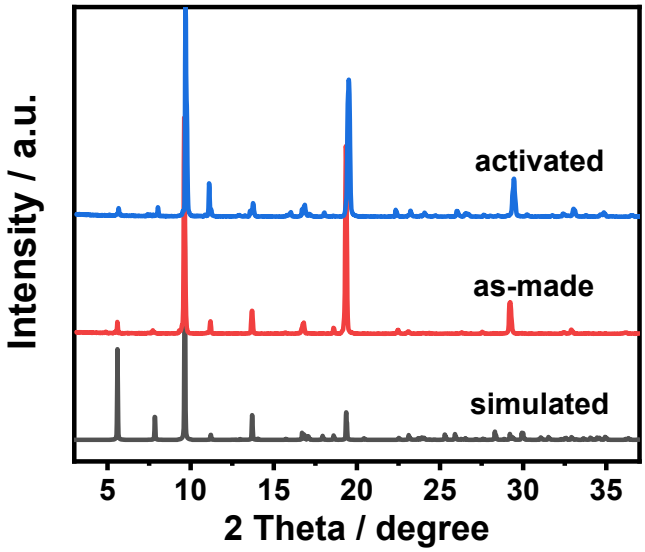

Fig. S2 The PXRD patterns of In(tcpp): simulated, as-made, and activated samples.

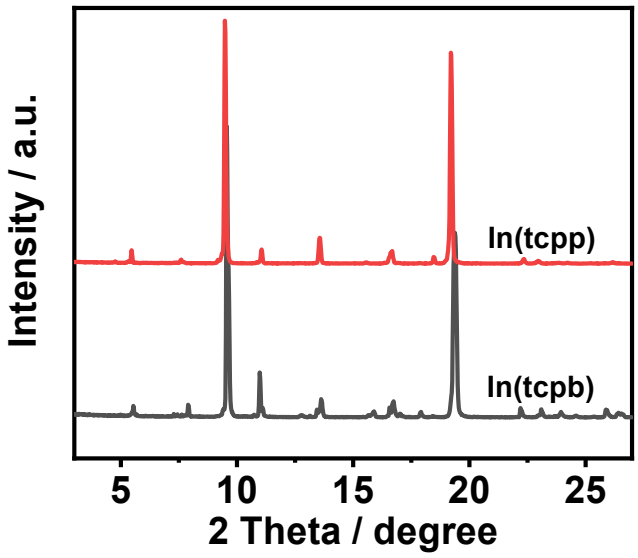

Fig. S3 The PXRD patterns of In(tcpp) and In(tcpb).

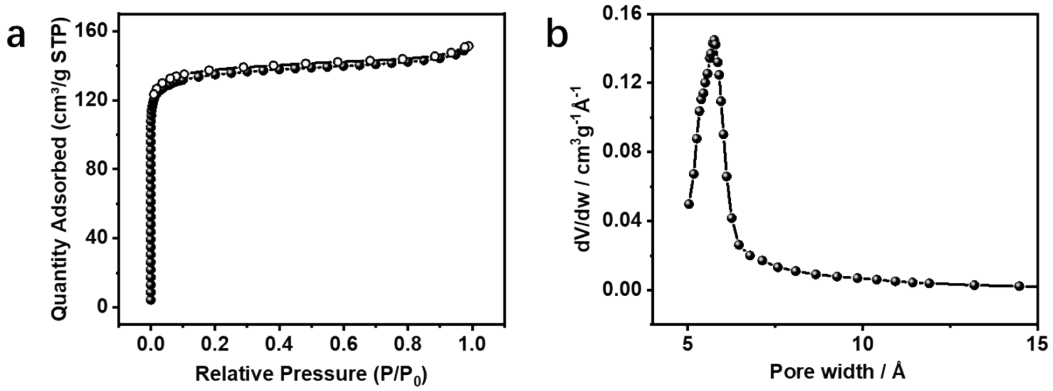

Fig. S4 (a) The N_2 adsorption and desorption isotherms of In(tcpp) collected at 77 K, adsorption: ●, de-sorption: ○. (b) The pore size distribution of In(tcpp).

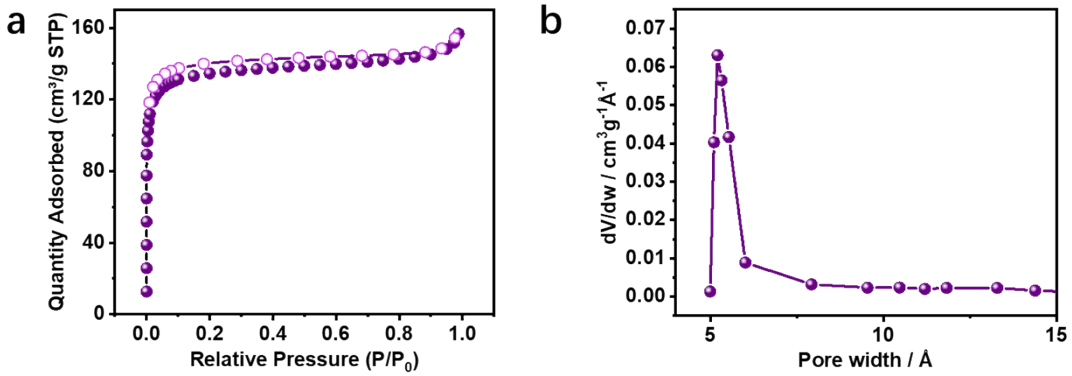

Fig. S5 (a) The BET adsorption and desorption isotherms for In(tcpb), adsorption: ●, de-sorption: ○. (b) The pore size distribution of In(tcpb).

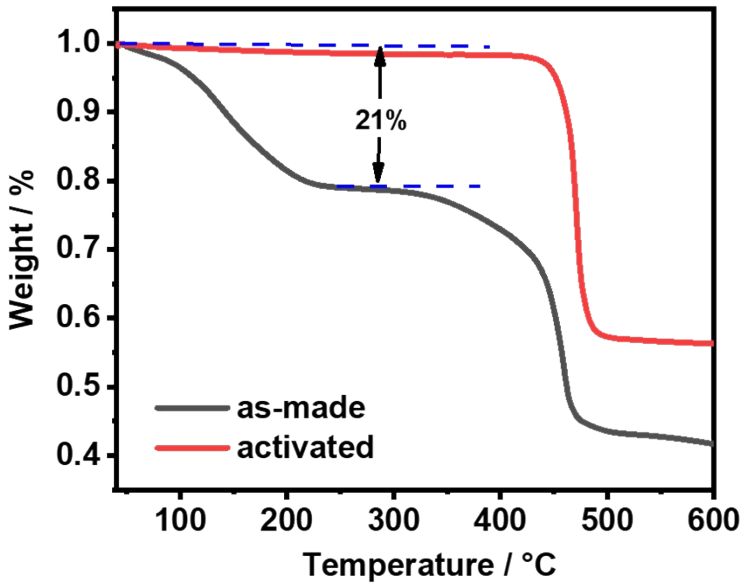

Fig. S6 Thermogravimetric (TG) profile of the as-made and activated In(tcpp) sample.

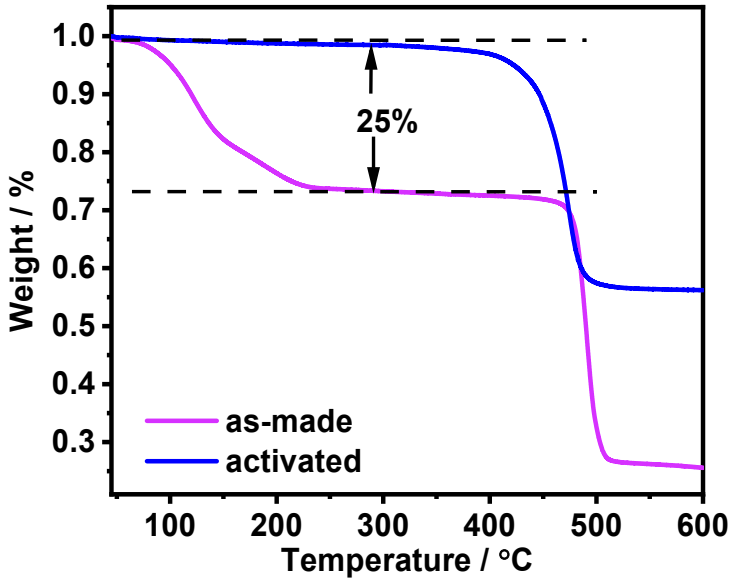

Fig. S7 TG profile of the as-made and activated In(tcpb) sample.

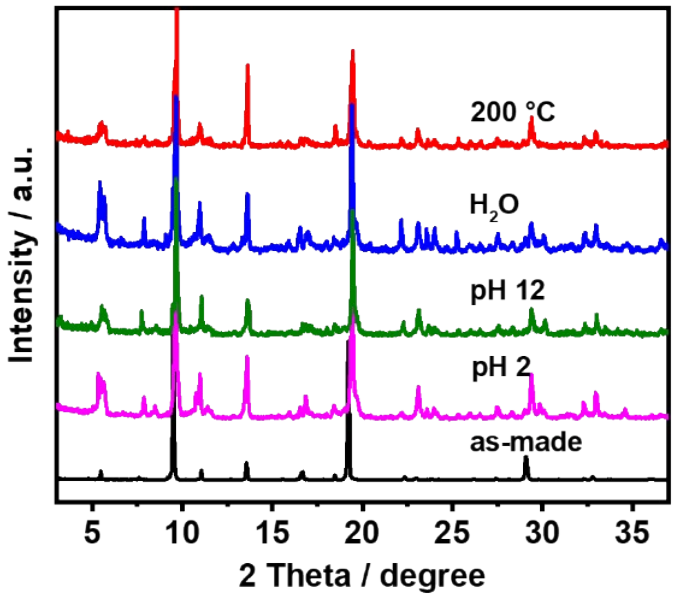

Fig. S8 The PXRD patterns of In(tcpp) after soaked in water, pH 2 and 12 solutions for 24 h, and heated at 200 °C for 2 h.

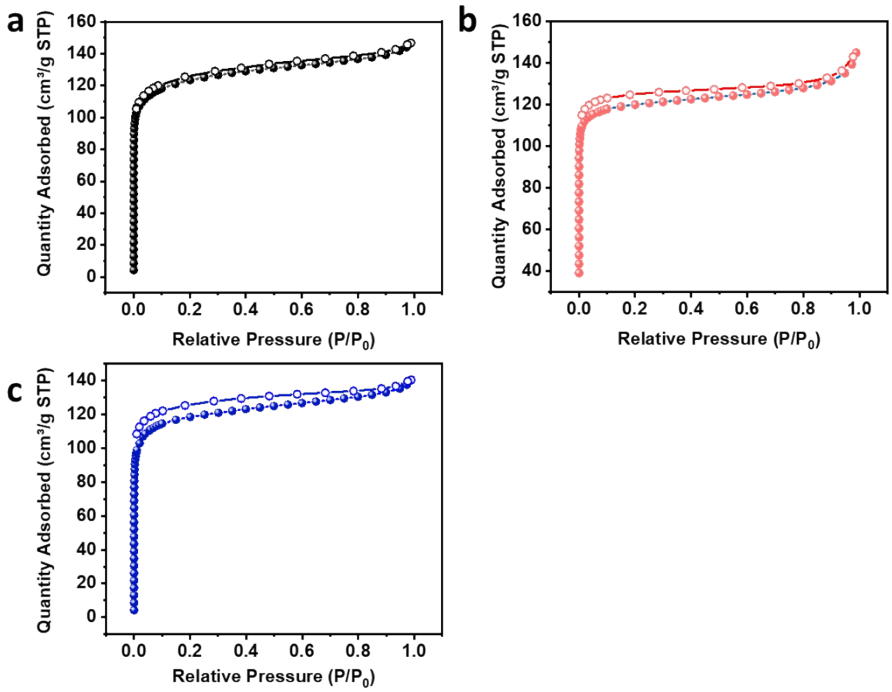

Fig. S9 The BET adsorption and desorption isotherms for In(tcpp), adsorption: ●, de-sorption: ○. (a) pH 2 (b) pH 10, and (c) 200 °C treated.

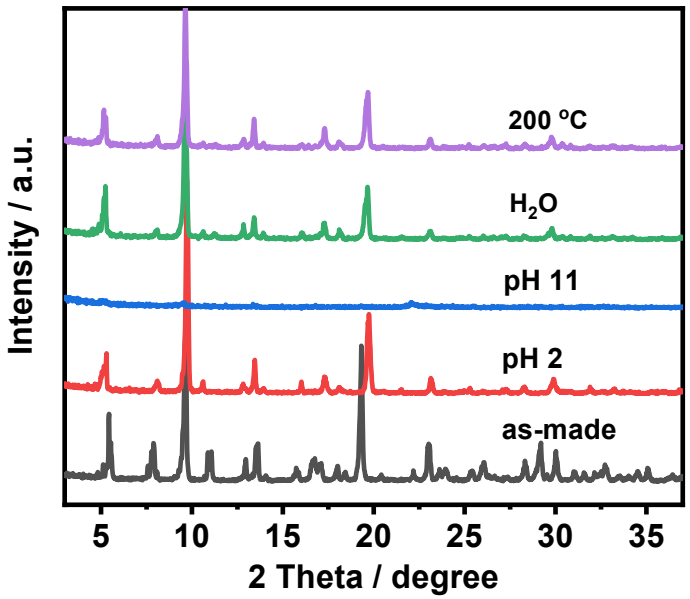

Fig. S10 PXRD patterns of the In(tcpb) sample after being soaked in water, pH 2 and pH 11 solutions for 24 h, or heated for 2 h at 200 °C.

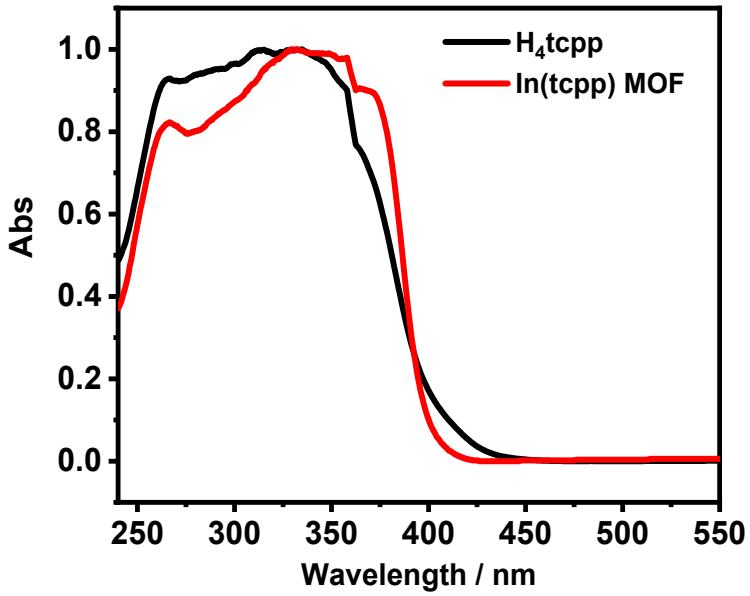

Fig. S11 UV-vis absorption spectra of the as-made In(tcpp) and H_4tcpp.

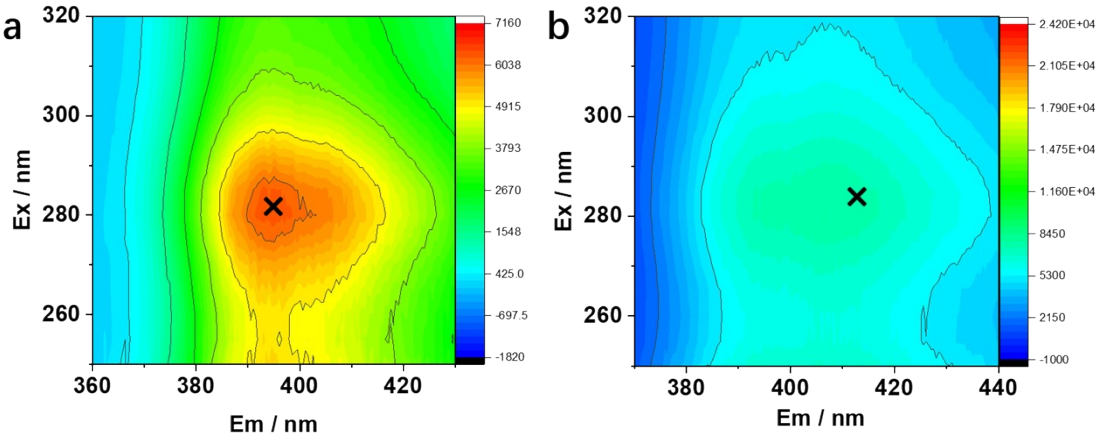

Fig. S12 The 3D mapping spectra of (a) In(tcpp) and (b) H_4tcpp to show the most suitable excitation and emission energies.

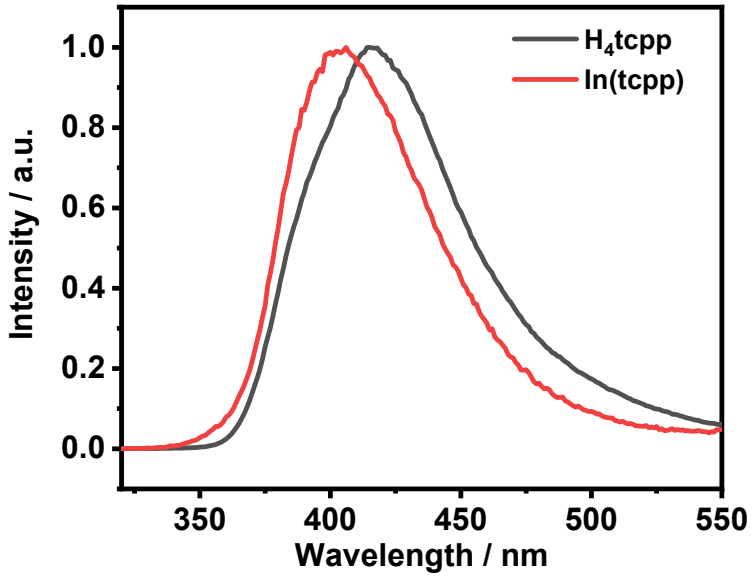

Fig. S13 The room temperature emission spectra of In(tcpp) and H_4tcpp under 280 nm excitation.

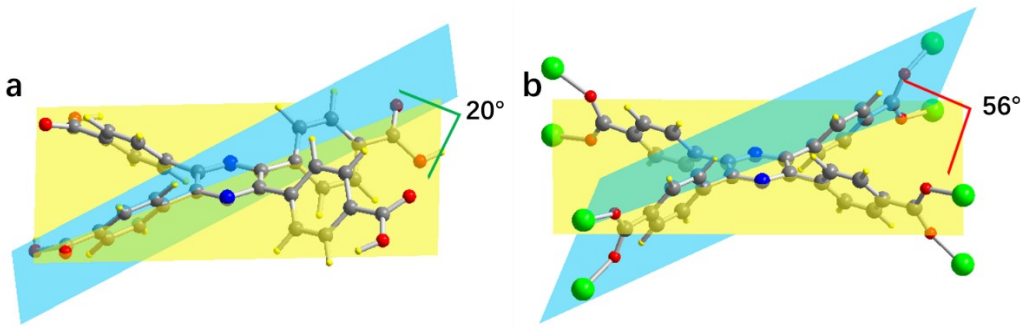

Fig. S14 The dihedral angle of (a) free H_4tcpp ligand and (b) tcpp in In(tcpp). (Color code: C, black; N, blue; O, red; In^{3+}, green; H, light yellow.)

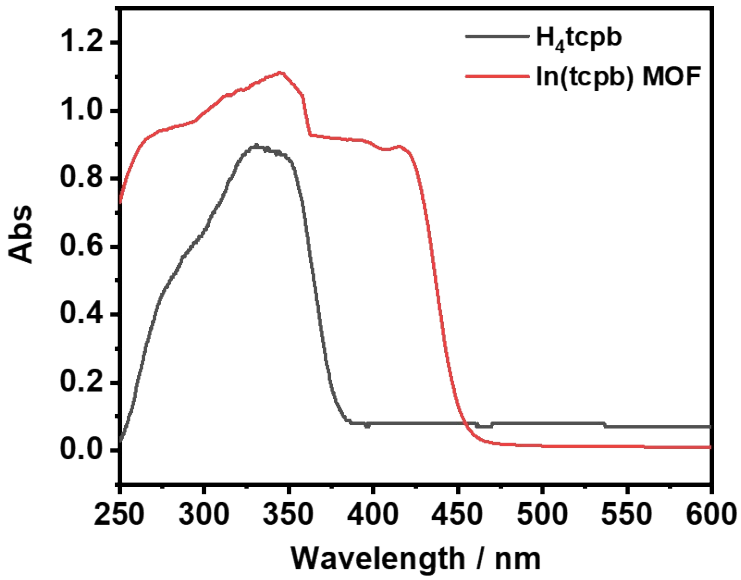

Fig. S15 UV-vis absorption spectra of In(tcpb) and H_4tcpb.

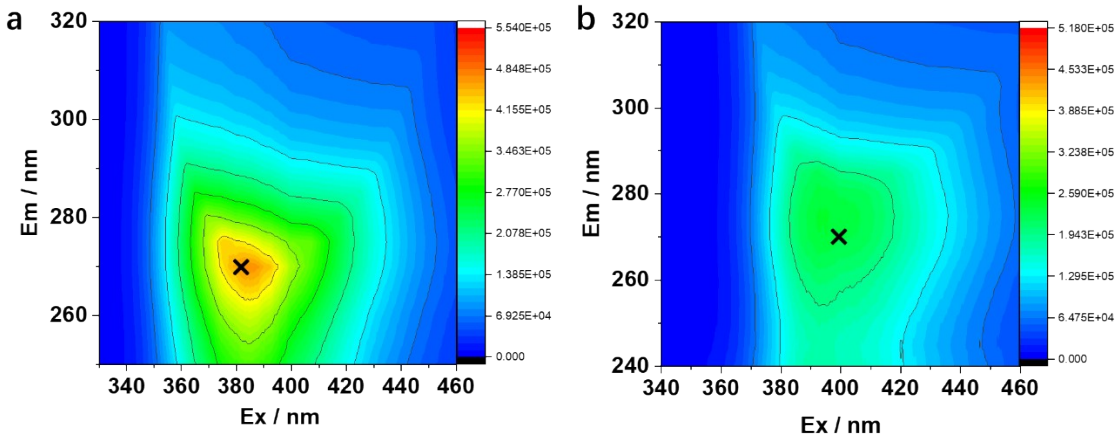

Fig. S16 The 3D PL mapping spectra of (a) In(tcpb) and (b) H_4tcpb.

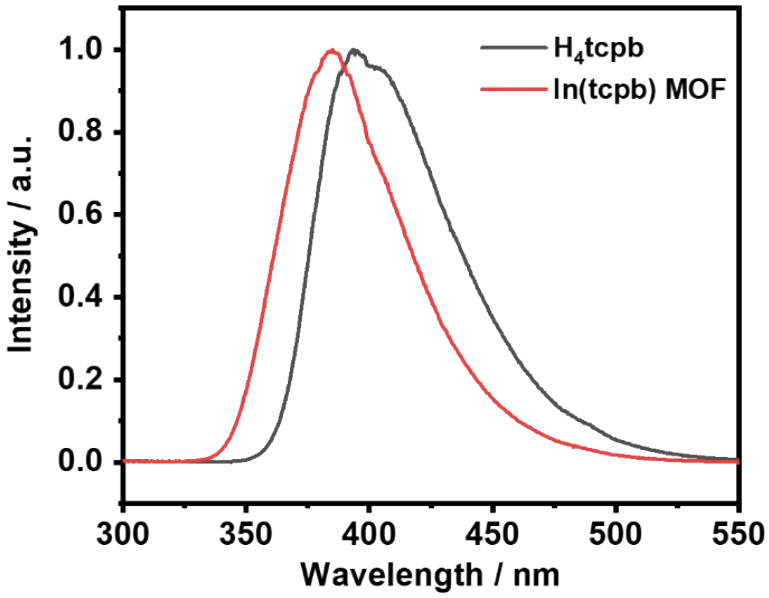

Fig. S17 The emission spectra of In(tcpb) and the ligand H_4tcpb under 270 nm excitation.

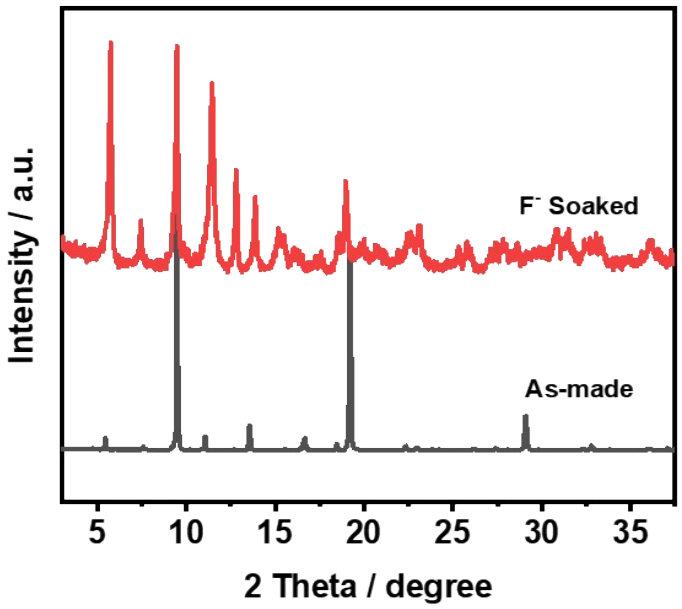

Fig. S18 PXRD patterns of (a) as-made In(tcpp), (b) In(tcpp) soaked in 1 mM F^- solution for 24 h.

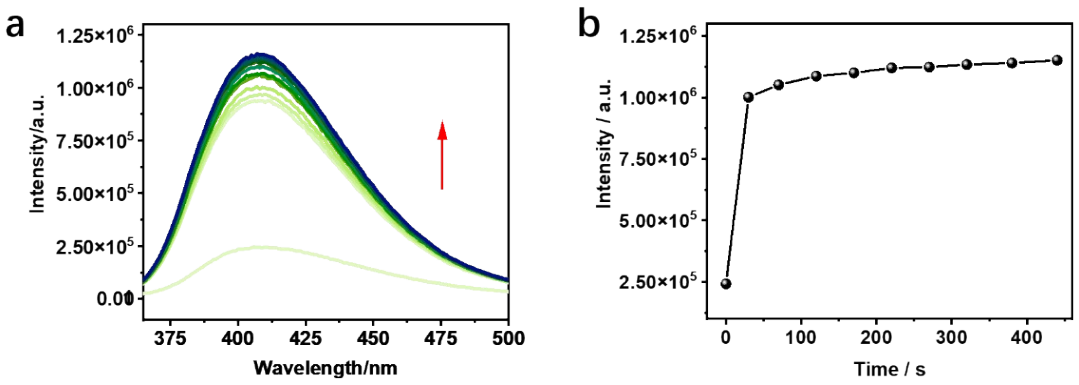

Fig. S19 The PL response of In(tcpp) to F^- as a function of time: (a) luminescence spectra and (b) the luminescence intensity.

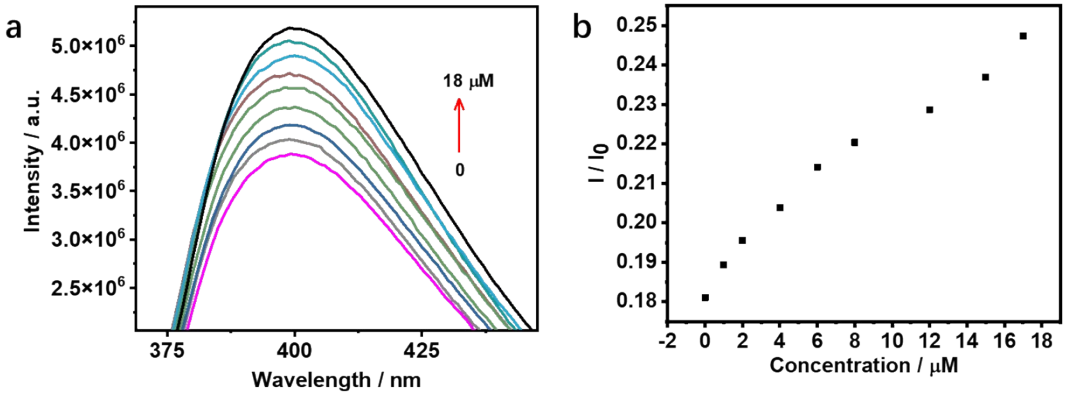

Fig. S20 (a) PL spectra of the In(tcpp) samples at low concentrations of F^- solution from luminescence titration experiments. (b) I/I_0 as a function of F^- concentration for samples in (a).

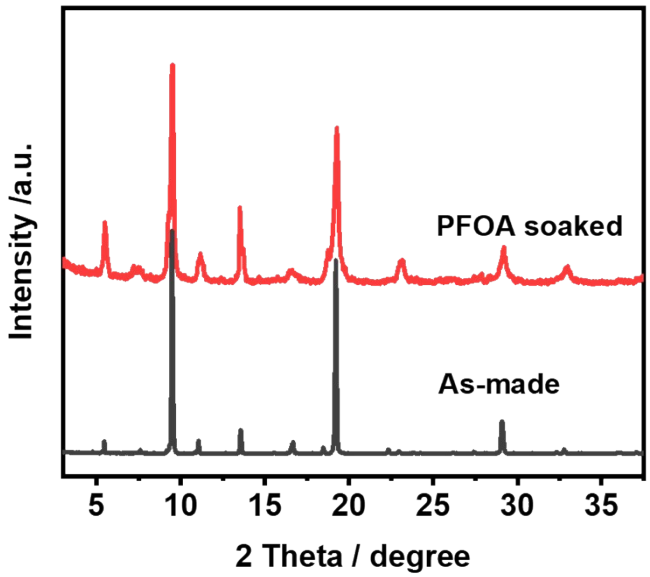

Fig. S21 PXRD overlay of the In(tcpp) samples, demonstrating the stability when exposed to PFOA of 1 mM.

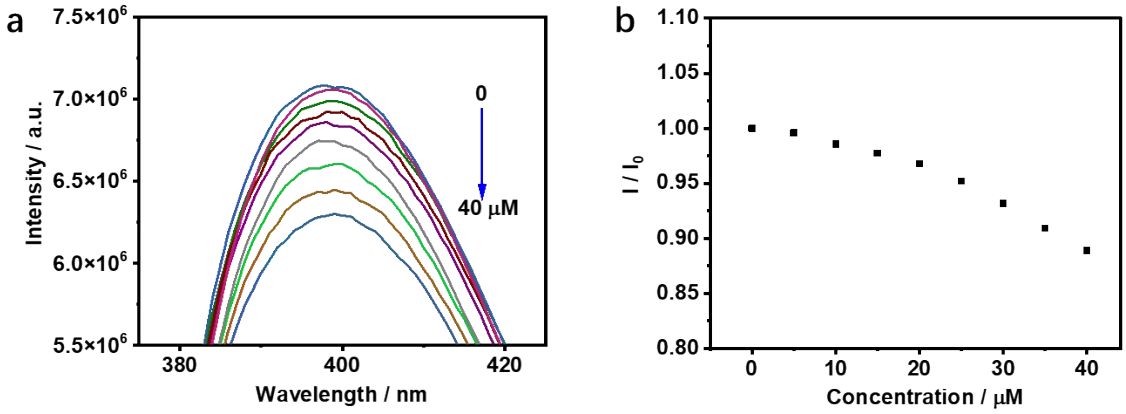

Fig. S22 (a) Emission spectra of In(tcpp) at low concentrations of PFOA solution. (b) The I/I_0 as a function of PFOA for samples in (a).

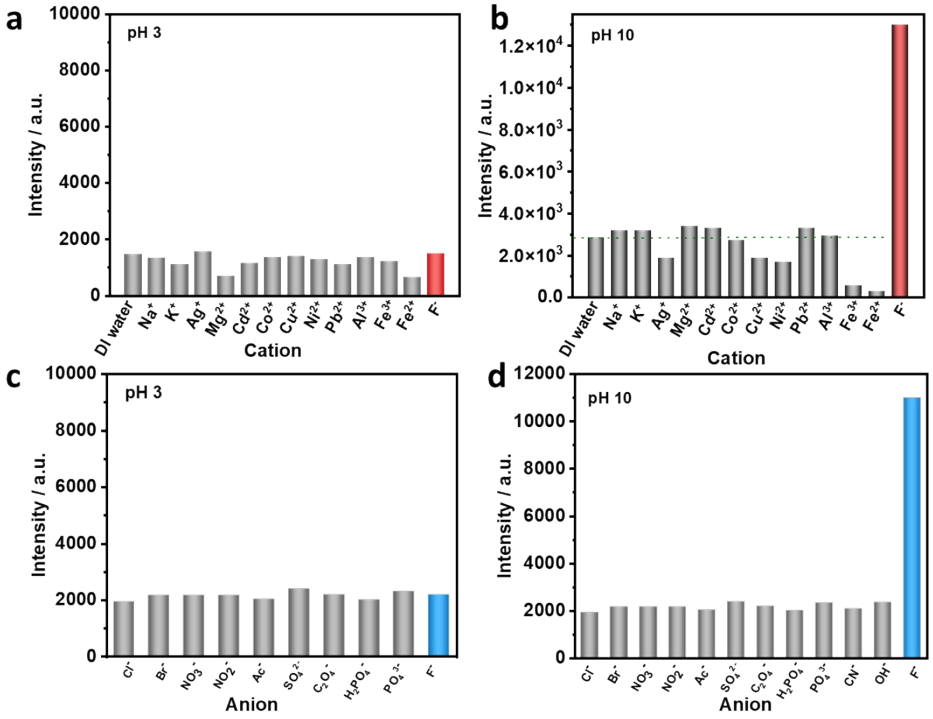

Fig. S23 The selectivity of F^- among different anions and cations (1 mM) in pH 3 and pH 10 solutions.

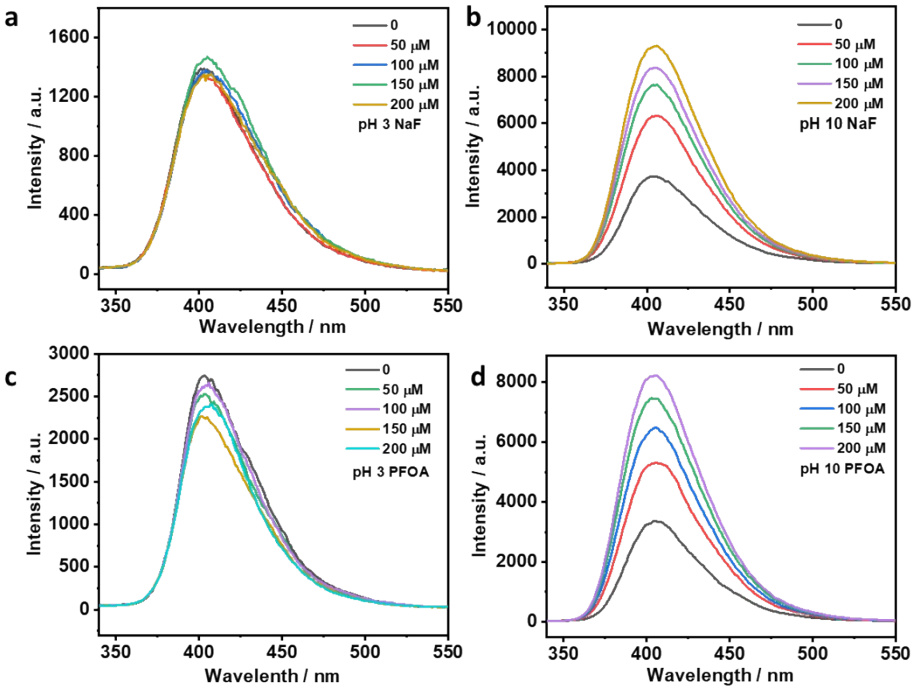

Fig. S24 The PL response of In(tcpp) to NaF in pH 3 and pH 10 solutions.

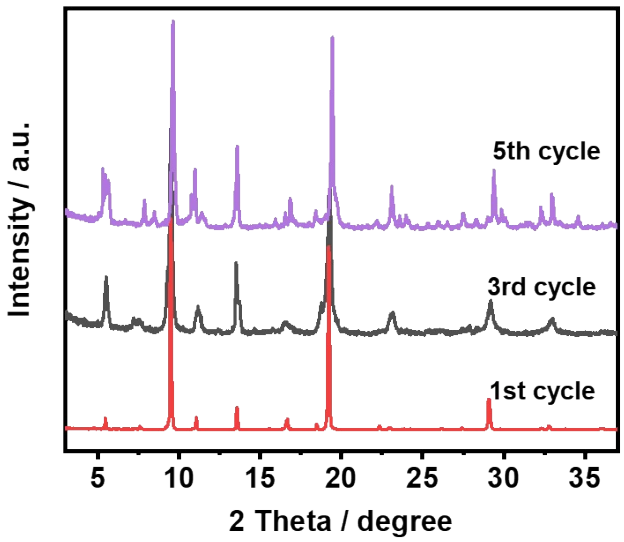

Fig. S25 The In(tcpp) PXRD patterns after five cycles F^- treated process.

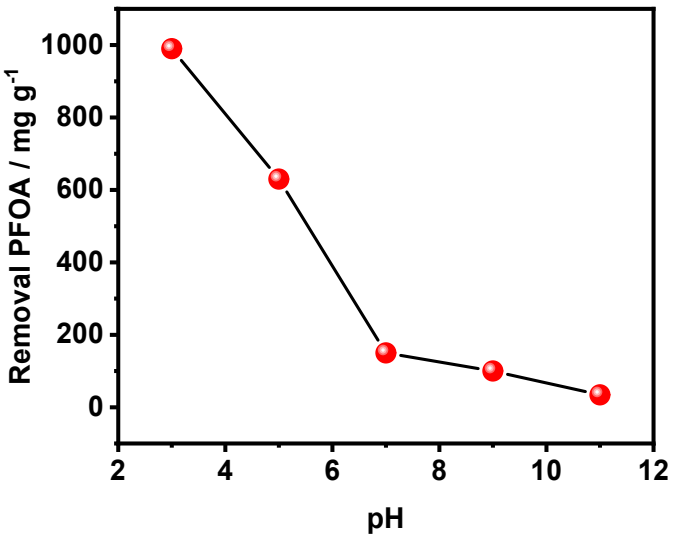

Fig. S26 The PFOA removal efficiency of In(tcpp) in different pH solutions.

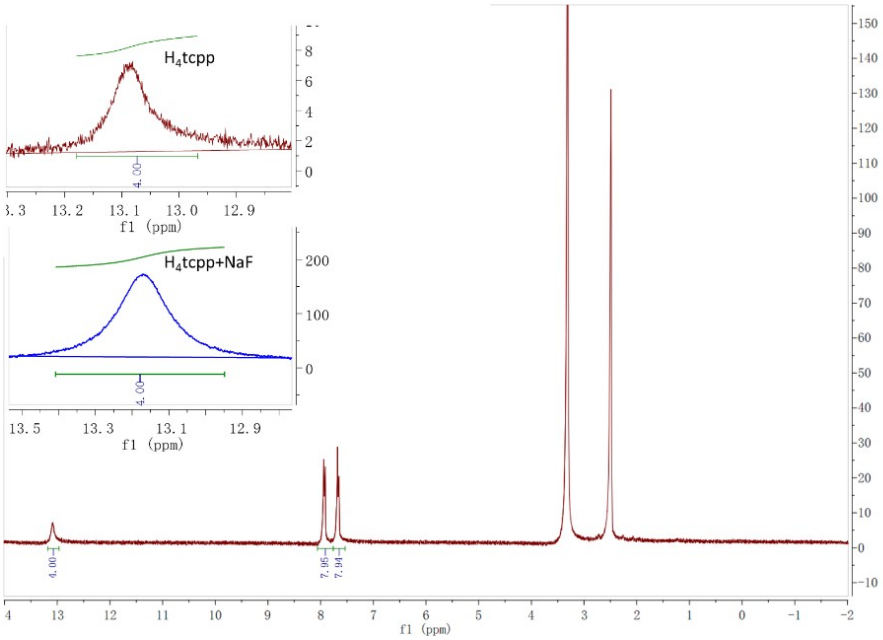

Fig. S27 The ^{1}H NMR of H_4tcpp before and after NaF addition.

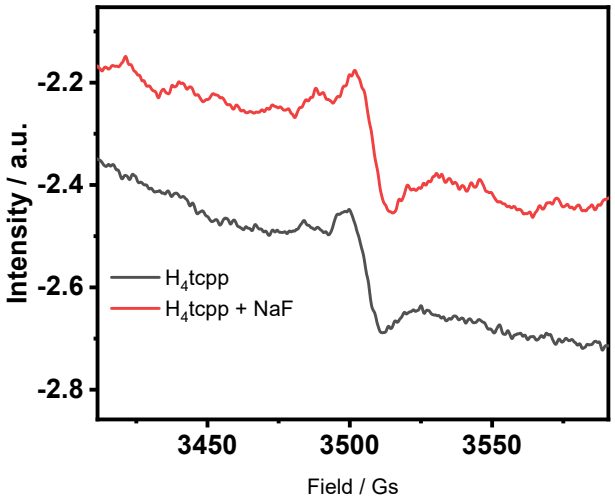

Fig. S28 The EPR spectra of H_4tcpp before and after NaF addition.

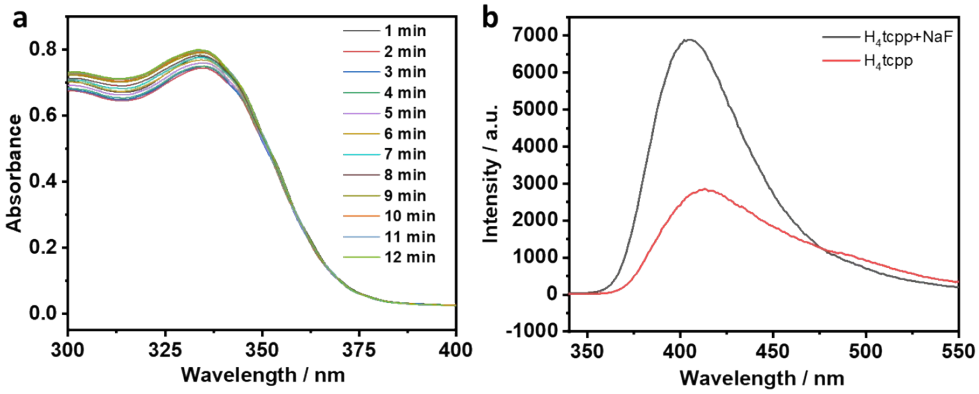

Fig. S29 The UV-vis and PL spectra of NaF response of In(tcpp).

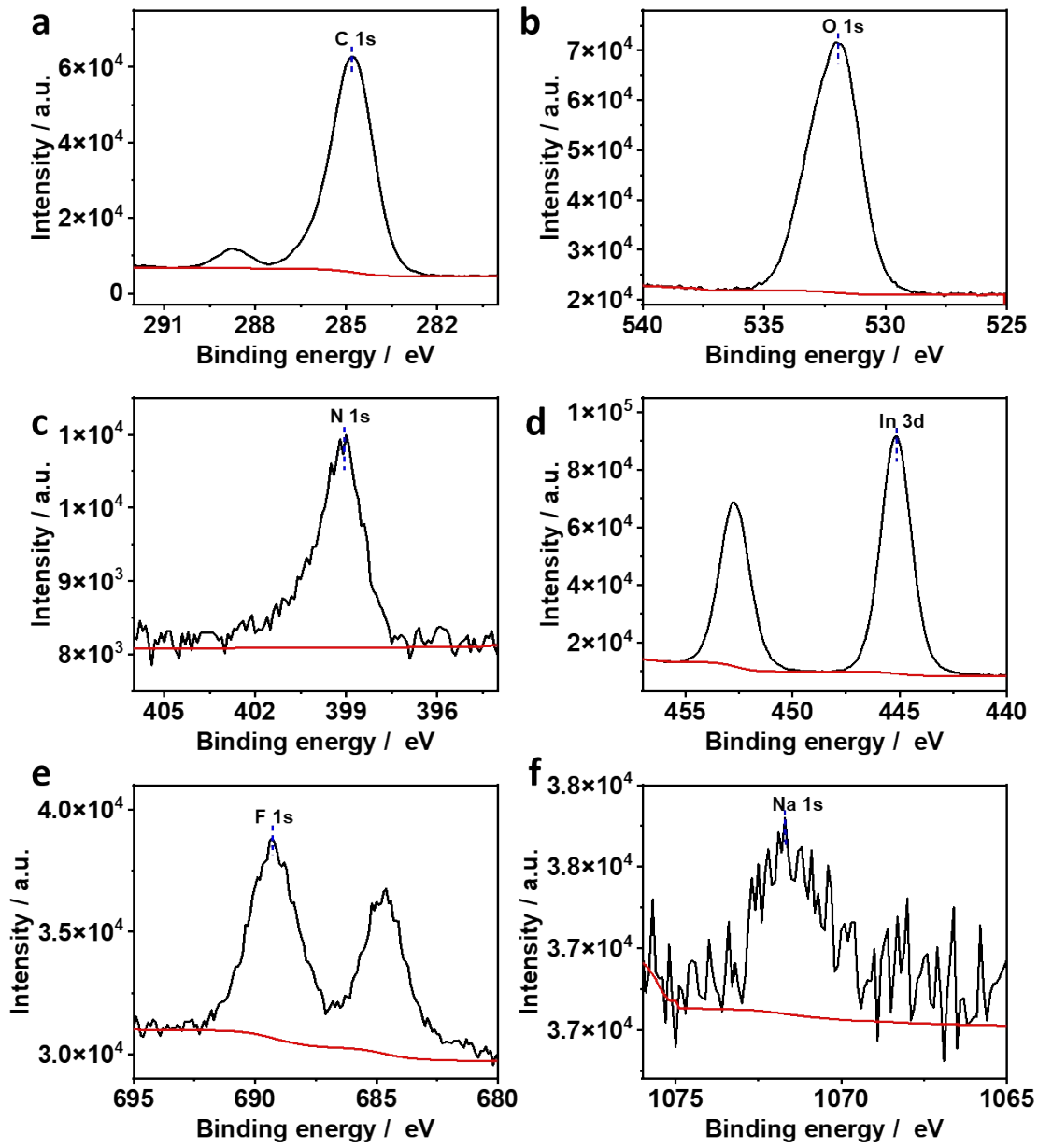

Fig. S30 XPS spectra of In(tcpp) sample after soaked in 0.5 mM NaF aqueous solution for 24 h.

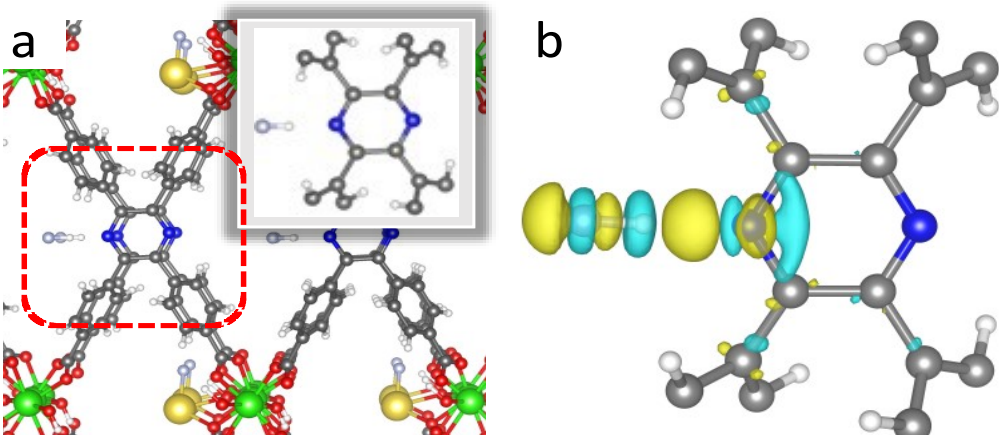

Fig. S31 (a) Optimized structure of HF@In(tcpp) highlighting H^+ and F- interactions. (b) The charge rearrangement (at an isolevel of 0.002 eV $Å^{-3}$) shows significant interaction of HF with N_{tcpp}.

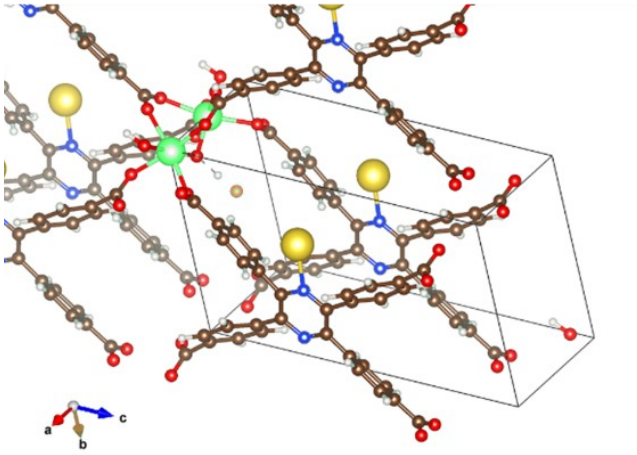

Fig. S32 Simulated interaction sites between NaF and In(tcpp). Na^+ interacts with the N_{tcpp} site, resulting in a positive binding energy (unfavorable adsorption).

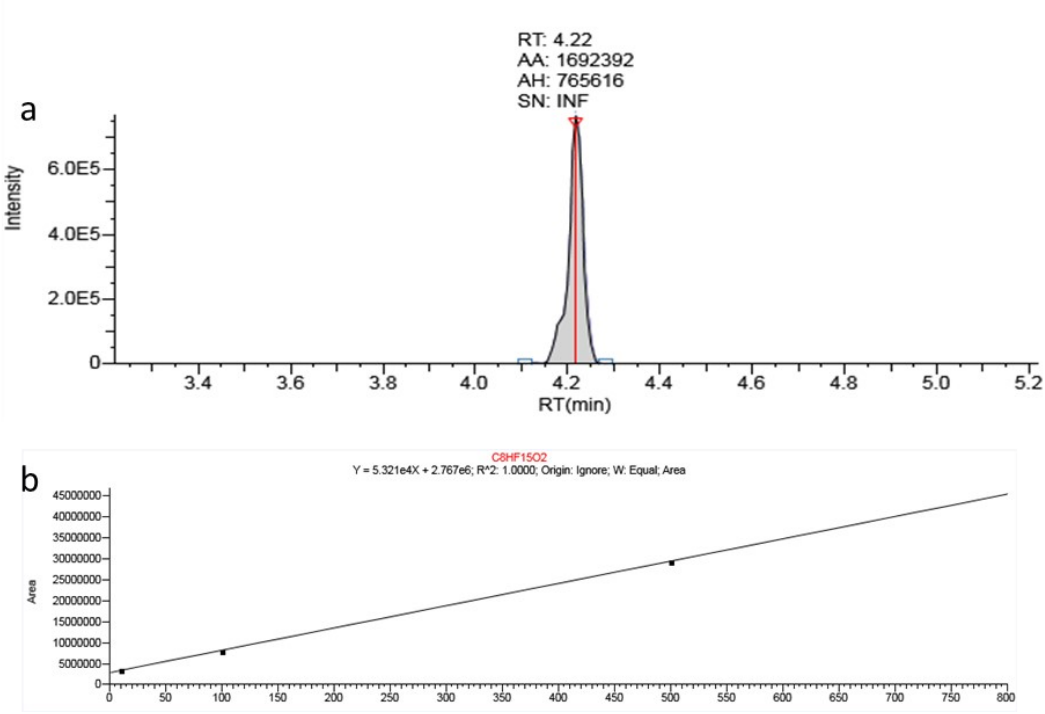

Fig. S33 (a) The HPLC-MS PFOA characteristic absorption peak. (b) The standard curve of PFOA of different concentration.

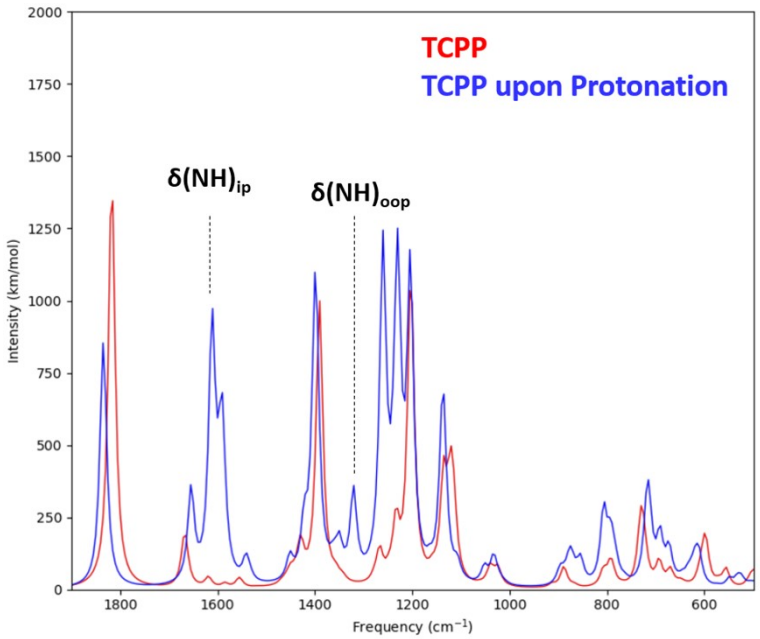

Fig. S34 Calculated IR spectra of tcpp and N protonated tcpp.

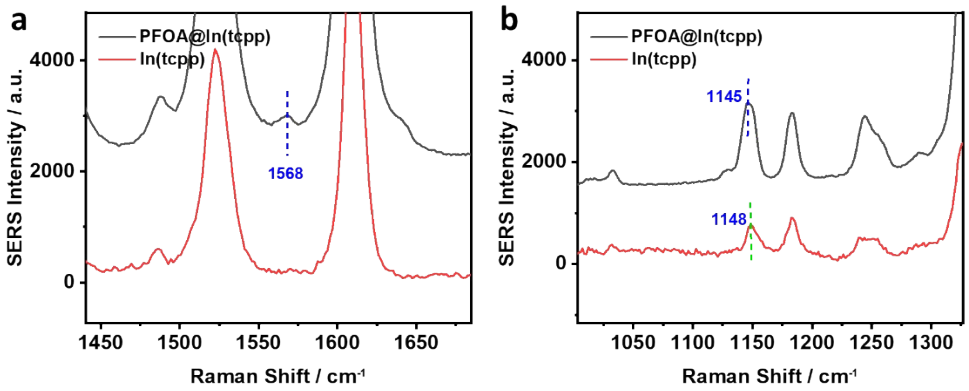

Fig. S35 The Raman spectra of PFOA@In(tcpp) and In(tcpp).

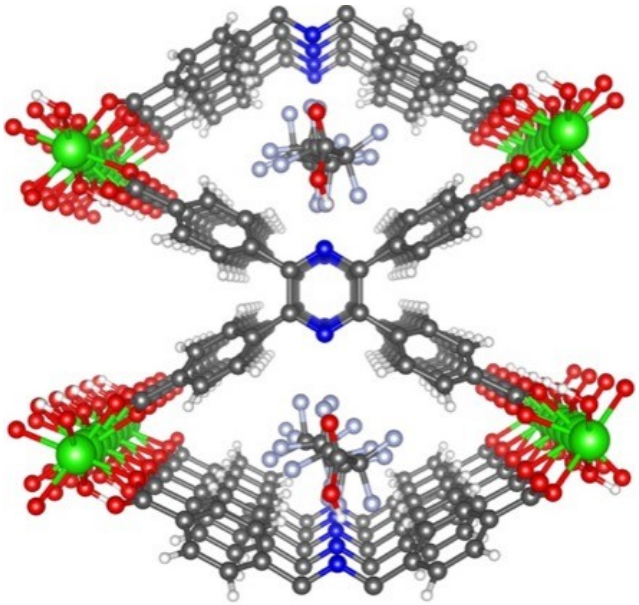

Fig. S36 Most favorable interaction configuration between PFOA and In(tcpp). PFOA mainly interacts with the N_{tcpp} linker via H bonding with a bond length of 1.48 Å. In addition, a similar interaction of the N_{tcpp} linker with an F@PFOA is also observed with a bond separation of 1.682 Å. Various other binding configurations were also considered, but we present here only the most favorable one.

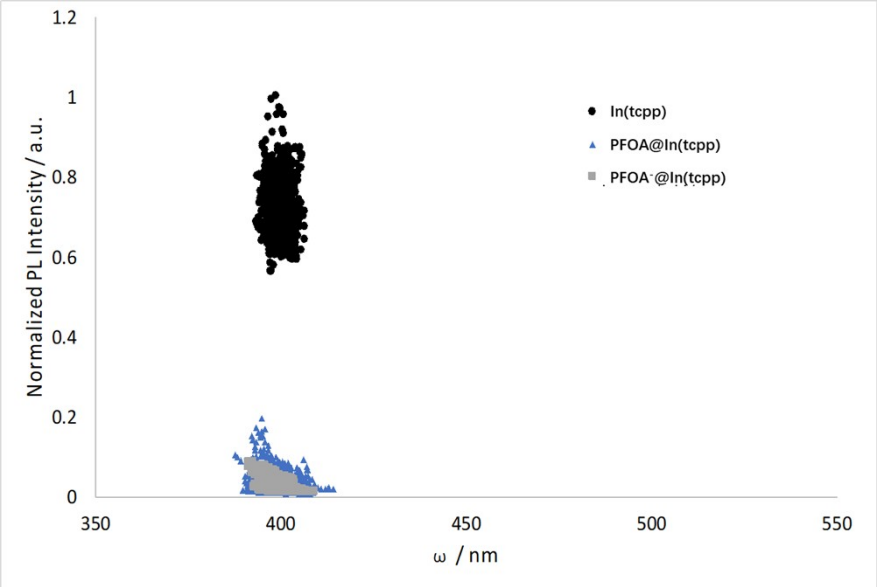

Fig. S37 Calculated photoluminescence intensity by using normalized oscillator strength values for In(tcpp) [black circles], PFOA@In(tcpp) [grey squares], and $PFOA^-$@In(tcpp) [blue triangles].

Table S1. The single crystal data of In(tcpp).

Empirical formula	$[In_2(tcpp)(OH)_2]$
Formula	$C_{16}H_9NO_5In$
Formula Weight	410.06
Temperature/K	298(2)
Crystal system	O
Space group	*Cmmm*
a/Å	7.2195(3)
b/Å	22.5222(10)
c/Å	15.7802(5)
α/°	90
β/°	90
γ/°	90
Volume/Å^3	2565.85(19)
Z	4
d_{calc}/g cm^{-3}	1.062
μ/mm^{-1}	0.987
F(000)	804.0
Radiation/Å	CuKα (λ =0.7288)
θ range for data collection/°	2.647 to 31.434
Index ranges	-9<=h<=10, -32<=k<=31, -22<=l<=22
Reflections collected	17781
Independent reflections	2229[R_{int} = 0.0738]
Data/restraints/parameters	2229/0/83
Goodness-of-fit on F^2	1.100
Final R indices [I>2sigma(I)]	R_1 = 0.0337, wR_2 = 0.0879
Final R indices (all data)	R_1 = 0.0394, wR_2 = 0.0942
Largest diff. peak and hole/e Å^{-3}	0.599 -0.674
CCDC No.	2057107

Empirical formula	$[In_2(tcpb)(OH)_2]$
Formula	$C_{34}H_{20}O_{10}In_2$
Formula Weight	818.14
Temperature/K	293.00(2)
Crystal system	Orthorhombic
Space group	*Cmmm*
a/Å	7.1852(2)
b/Å	22.1619(7)
c/Å	16.1168(5)
α/°	90
β/°	90
γ/°	90
Volume/Å^3	2566.40(13)
Z	2
d_{calc}/g cm^{-3}	1.059
μ/mm^{-1}	7.490
F(000)	804.0
Radiation/Å	CuKα (λ = 1.54184)
θ range for data collection/°	3.9680 to 78.3950
Index ranges	-4<=h<=8, -23<=k<=27, -20<=l<=17
Reflections collected	4842
Independent reflections	1566[R_{int} = 0.0331]
Data/restraints/parameters	1566/8/65
Goodness-of-fit on F^2	1.320
Final R indices [I>2sigma(I)]	R_1 = 0.0463 , wR_2 = 0.1688
Final R indices (all data)	R_1 = 0.0503 , wR_2 = 0.1742
Largest diff. peak and hole/e Å^{-3}	1.393 - 1.252
CCDC No.	2057106

Table S2. The single crystal data of In(tcpb).

Table S3. LODs of different materials used for luminescence-based F^- detection.

Name	Materials type	LOD	Ref.
SION-105	MOFs	0.1 ppm	11
Eu-MOF 1	MOFs	2 μM	12
NH_2–MIL–101(Al)@DCF	MOFs	0.05 μM	13
2-(thiazolyl-2-salicylaldimine)coumarin	molecule	0.11 μM[#1]	14
(E)-2-[(pyridin-2ylimino)methyl]phenol	molecule	14 pM	15
4-Methyl Halide Phenolate Derivatives	molecule	25 μM[#2]	16
Probe I	molecule	73 nM	17
Mito-PF	molecule	4.642 uM[#3]	18
sensor L	molecule	0.806 μM	19
MPIPIC	molecule	0.02 mg L^{-1}	20
APBA-CuInS2 QDs	quantum dots	1.2 μmol L^{-1}	21
CDs/-cd	quantum dots	~6.6 μM.	22
DL-PQDs	quantum dots	3.2 μM	23
AgNP-MPBA	graphene oxide	9.07 pM	24
GO-Fe (III)	graphene oxide	1.0 pM	25
TPA	nanozymes	0.64 μM	26
CeO_2 nanozyme	nanozymes	1.8 μM	27
MPBA-AuNPs	nanoparticles	0.345 μM	28

Note: [#]1 in MeCN, [#]2 in DMSO/ACN/H_2O, [#]3 in DMSO/PBS.

Table S4. LODs of different types of materials used for perfluorinated pollutants detection.

Name	Material type	LOD	Ref.
F-MOF	MOFs	2.6 ng L^{-1}	29
UCNPs	COFs	0.15 pM	30
Guanidinocalix[5]arene	molecule	26.4 ±0.2 nM	31
TPE-chip	molecule	~0.2 ppb[&]	32
SeN-CQDs	quantum dots	1.8 μM	33
CdTe@CdS QDs	quantum dot	25 nM	34
MoS_2/Fe_3O_4	nanocomposites	8.6 nM	35
MIP@AgI–BiOINFs	hybrid	0.01 ppb	36
smartphone APP	Reading-kit and APP	0.5 ppb	37

[&] in acetone/water

Table S5. Elemental analysis based on XPS spectra of NaF@In(tcpp).

Elements	Area CPS / eV	Atomic %
C 1s	112792.75	60.15
N 1s	7054.48	2.33
O 1s	133672.43	26.93
In 3d	254130.54	4.43
F 1s	38528.66	5.83
Na 1s	4442.93	0.34

Table S6. Experimental and calculated vibrational frequencies for F^- in In(tcpp).

Vibrational Mode	Frequency / cm^{-1}	
	In(tcpp)	Na^+F^-@In(tcpp)
	Computational/Experimental	Computational/Experimental
O-H Stretch	3838/3698	2153/not detected
O-H Bend	1004/988	1271/1301

References

1. H. Q. Yin, X. Y. Wang and X. B. Yin, *J. Am. Chem. Soc.*, 2019, **141**, 15166-15173.
2. G. Kresse and D. Joubert, *Phys. Rev. B*, 1999, **59**, 1758-1775.
3. G. Kresse and J. Furthmüller, *Phys. Rev. B*, 1996, **54**, 11169-11186.
4. K. Berland, V. R. Cooper, K. Lee, E. Schröder, T. Thonhauser, P. Hyldgaard and B. I. Lundqvist, *Rep. Prog. Phys.*, 2015, **78**, 066501.
5. D. C. Langreth, B. I. Lundqvist, S. D. Chakarova-Käck, V. R. Cooper, M. Dion, P. Hyldgaard, A. Kelkkanen, J. Kleis, L. Kong, S. Li, P. G. Moses, E. Murray, A. Puzder, H. Rydberg, E. Schröder and T. Thonhauser, *J. Phys.: Condens. Matter*, 2009, **21**, 084203.
6. T. Thonhauser, V. R. Cooper, S. Li, A. Puzder, P. Hyldgaard and D. C. Langreth, *Phys. Rev. B*, 2007, **76**, 125112.
7. T. Thonhauser, S. Zuluaga, C. A. Arter, K. Berland, E. Schroder and P. Hyldgaard, *Phys. Rev. Lett.*, 2015, **115**, 136402.
8. D. J. Vogel and D. S. Kilin, *J. Phys. Chem. C*, 2015, **119**, 27954-27964.
9. S. Jensen, K. Tan, W. P. Lustig, D. S. Kilin, J. Li, Y. J. Chabal and T. Thonhauser, *Chem. Mater.*, 2019, **31**, 7933-7940.
10. S. Jensen, K. Tan, W. Lustig, D. Kilin, J. Li, Y. J. Chabal and T. Thonhauser, *J. Mater. Chem. C*, 2019, **7**, 2625-2632.
11. F. M. Ebrahim, T. N. Nguyen, S. Shyshkanov, A. Gladysiak, P. Favre, A. Zacharia, G. Itskos, P. J. Dyson and K. C. Stylianou, *J. Am. Chem. Soc.*, 2019, **141**, 3052-3058.
12. Z.-R. Yang, M.-M. Wang, X.-S. Wang and X.-B. Yin, *Anal. Chem.*, 2017, **89**, 1930-1936.
13. Y. Sun, X. Xu, Y. Zhao, H. Tan, Y. Li and J. Du, *Talanta*, 2020, **209**, 120582.
14. S. S. Razi, P. Srivastava, R. Ali, R. C. Gupta, S. K. Dwivedi and A. Misra, *Sens. Actuators B Chem.*, 2015, **209**, 162-171.
15. P. Alam, V. Kachwal and I. Rahaman Laskar, *Sens. Actuators B Chem.*, 2016, **228**, 539-550.
16. L. Gabrielli and F. Mancin, *J. Org. Chem.*, 2016, **81**, 10715-10720.
17. X. Wu, H. Wang, S. Yang, H. Tian, Y. Liu and B. Sun, *ACS Omega*, 2019, **4**, 4918-4926.
18. J. Ji, Z. Zhang, F. Zhan, Q. Wang and G. Zheng, *J. Photochem. Photobiol. A Chem.*, 2020, **390**, 112349.
19. L. Xiao, L. Ren, X. Jing, Z. Li, S. Wu and D. Guo, *Inorg. Chim. Acta*, 2020, **500**, 119207.
20. A. Das, S. U. Dighe, N. Das, S. Batra and P. Sen, *Spectrochimica acta. Part A, Molecular and biomolecular spectroscopy*, 2019, **220**, 117099.
21. Z. Liu, L. Liu, M. Sun and X. Su, *Biosens. Bioelectron.*, 2015, **65**, 145-151.
22. U. Baruah, N. Gogoi, G. Majumdar and D. Chowdhury, *Carbohydr. Polym.*, 2015, **117**, 377-383.
23. L.-Q. Lu, M.-Y. Ma, T. Tan, X.-K. Tian, Z.-X. Zhou, C. Yang and Y. Li, *Sens Actuators B Chem.*, 2018, **270**, 291-297.
24. X. Chen, S. Yu, L. Yang, J. Wang and C. Jiang, *Nanoscale*, 2016, **8**, 13669-13677.
25. T. K. Mandal, Y. Hou, Z. Gao, H. Ning, W. Yang and M. Gao, *Adv Sci (Weinh)*, 2016, **3**, 1600217.
26. B. Liu, Z. Huang and J. Liu, *Nanoscale*, 2016, **8**, 13562-13567.
27. D. Li, S. L. Garisto, P.-J. J. Huang, J. Yang, B. Liu and J. Liu, *Inorg. Chem. Commun.*, 2019, **106**, 38-42.
28. H. Wu, Y. Li, X. He, L. Chen and Y. Zhang, *Spectrochim. Acta A Mol. Biomol. Spectrosc.*, 2019, **214**, 393-398.
29. S. Y. Ma, J. Wang, L. Fan, H. L. Duan and Z. Q. Zhang, *J. Chromatogr. A*, 2019, DOI: 10.1016/j.chroma.2019.460616, 460616.
30. J. Li, C. Zhang, M. Yin, Z. Zhang, Y. Chen, Q. Deng and S. Wang, *ACS Omega*, 2019, **4**, 15947-15955.
31. Z. Zheng, H. Yu, W. C. Geng, X. Y. Hu, Y. Y. Wang, Z. Li, Y. Wang and D. S. Guo, *Nat. Commun.*, 2019, **10**, 5762.
32. C. Fang, J. Wu, Z. Sobhani, M. A. Amin and Y. Tang, *Anal. Methods*, 2019, **11**, 163-170.
33. L. S. Walekar, M. Zheng, L. Zheng and M. Long, *Mikrochim. Acta*, 2019, **186**, 278.
34. L. Zheng, Y. Zheng, Y. Liu, S. Long, L. Du, J. Liang, C. Huang, M. T. Swihart and K. Tan, *Talanta*, 2019, **194**, 1-6.
35. J. Liu, J. Du, Y. Su and H. Zhao, *Microchem. J.*, 2019, **149**, 104019.
36. J. Gong, T. Fang, D. Peng, A. Li and L. Zhang, *Biosens. Bioelectron.*, 2015, **73**, 256-263.
37. C. Fang, X. Zhang, Z. Dong, L. Wang, M. Megharaj and R. Naidu, *Chemosphere*, 2018, **191**, 381-388.